INVITED PAPER *Special Section on Recent Progress in Active Photonic Device Technologies*

Metal-Cavity Nanolasers and NanoLEDs

Shun Lien CHUANG[†a)], **Chi-Yu NI**[†], **Chien-Yao LU**[†], *and* **Akira MATSUDAIRA**[†], *Nonmembers*

SUMMARY We present the theory and experiment of metal-cavity nanolasers and nanoLEDs flip-chip bonded to silicon under electrical injection at room temperature. We first review the recent progress on micro- and nanolasers. We then present the design rule and our theoretical model. We show the experimental results of our metal-cavity surface-emitting microlasers and compare with our theoretical results showing an excellent agreement. We found the important contributions of the nonradiative recombination currents including Auger recombination, surface recombination, and leakage currents. Finally, experimental demonstration of electrical injection nanoLEDs toward subwavelength nanoscale lasers is reported.

key words: *nanolasers, nanoLEDs, microcavity, plasmonic waveguides, metal cavity*

1. Introduction

There has been intensive research on subwavelength nanoscale lasers for potential applications in future generation optical interconnects, optical data storage, and high resolution biochemical imaging [1]–[3]. Since the invention of the laser [4] and semiconductor lasers [5]–[8], the size of lasers has been reduced significantly. The vertical-cavity surface-emitting lasers (VCSELs) [9], microdisk lasers [10], and the photonic crystal nanolasers [11] have reduced the size of the laser toward an ultra small cavity volume although the physical sizes are still a few wavelengths in three dimensions. To push the size of the lasers below the diffraction limit (i.e., a size of a half wavelength in all three directions), a recent work of a naolaser with a diameter of 210 nm and a height of 1.5 mm has been realized with electrical injection at 10 K [12]. To achieve operation at room temperature, a cavity of 300 nm in width and 6 mm in length [13] has been demonstrated with pulsed operation. A continuous wave (CW) mode laser with a similar size has also been realized [14]. A metallo-dielectric pedestal pillar laser with further size reduction was made with thicker optical buffer layers [15]. Optically pumped metal-cavity nano-patch lasers at 77 K [16], nano-pan lasers at 8 K [17], and nanolasers at 300 K [18] further decreased the size to subwavelength in three dimensions. Hybrid structures incorporating photonic crystals and metals are also proposed and investigated [19], [20]. The advantages of metal-cavity nanolasers and nanoLEDs are to provide an ultrasmall cavity volume with low power consumption, ultrahigh speed modulation, and ultra-high density photonic integration for intrachip optical interconnect. In contrast, microdisk lasers are restricted by the diffraction limit. Although the photonic crystal lasers can effectively produce a small effective modal volume, still, they require an area with a radius of several micrometers in order to have a significant quality factor. Therefore, metal-cavity nanolasers and nanoLEDs provide the potential for true reduction of cavity volume with potential high performance. The use of metals to increase mirror reflectivity for lasers can be traced back to the first ruby laser by Maiman [4]. Iga's invention of VCSEL [9] also used a 50-μm metal aperture as a reflector, while reducing the vertical size greatly. We have recently developed a fundamental formulation for nanoscale lasers taking into account the plasmonic dispersion of the metals and the negative permittivity in metal cavity structures [21]–[23]. Metal-cavity surface-emitting microlasers have also been proposed and demonstrated experimentally [24]–[27] showing continuous-wave (CW) operation at room temperature. Nanoscale LEDs with electrical injection have also been demonstrated [28], paving the way toward subwavelength nanolasers.

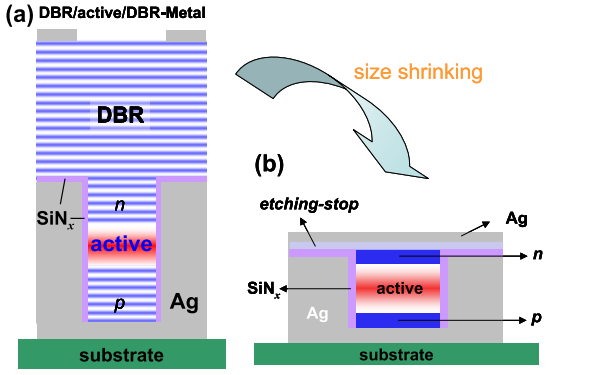

Fig. 1 (a) The proposed metal-cavity surface-emitting laser structure with top and bottom DBR pairs. The GaAs substrate is removed with a flip-chip bonding to the receptor (silicon) substrate. Metals (silver) are used to conformally coat the lithographically defined semiconductor structure to form a metal cavity. An active region using quantum wells is placed in between carrier injection layers. The device emits light vertically through the top surface and is circular in shape. [24]–[27] (b) Proposal of a nanocoin laser structure using bulk active region surrounded by a metal cavity [30].

Our surface-emitting configuration, Fig. 1(a), for metal-cavity nanolasers [24]–[27] consists of a few innovations compared to other metal-cavity lasers [29]. Our

Manuscript received November 30, 2011.
Manuscript revised January 27, 2012.

[†]The authors are with the Department of Electrical and Computer Engineering, the University of Illinois at Urbana-Champaign, 1406 West Green Street, Urbana, Illinois, 61801, USA.
a) E-mail: s-chuang@illinois.edu

DOI: 10.1587/transele.E95.C.1235

design is based on the HE_{11} mode of a metal-coated insulator-semiconductor (core) coaxial structure with a circular beam shape, top-emitting design, which is ideal for laser sources compared to the slit or rectangular window of other nanolasers, which usually introduces optical field distortion in certain directions. For a detailed comparison of our design using the propagation mode with others such as those using a cutoff mode structure for feedback, see [29]. Our devices require the substrate removal to reduce the propagation loss of the light output through a thick substrate and to reduce the heating effects [26]. The complete metal encapsulation and flip-chip bonding to a silicon substrate improve the optical mode confinement, provide efficient heat removal, and most importantly, isolate individual devices from cross talk for high density photonic integration. We have demonstrated CW room temperature operation for both 870 nm and 995 nm lasing wavelengths microlasers, moving toward nanoscale lasers.

Figure 1(b) shows our proposal of a nanocoin laser for further size reduction by removing the DBR reflectors. In this paper, we present the progress on our proposed room temperature metal-cavity surface-emitting microlasers [27] and nanoLEDs [28], which operate in continuous-wave (CW) mode with electrical injection. We also show new theoretical results based on our theoretical model and comparison with experimental data with a very good agreement. We identify the contributions of radiative vs. non-radiative recombination currents, such as Auger recombination, defect recombination, and leakage current, as a function of the injection current. We then present our conclusion and future work.

2. Theory of Nanolasers

2.1 Design Rules

To satisfy the lasing condition for a laser, the phase and the threshold conditions have to be met simultaneously. Similar to previous work [31] on our first generation metal-cavity nanolasers [24], [25], the round trip phase condition $\Phi(\omega)=2m\pi$ and the net threshold modal gain condition $G(g)=0$ of a transverse mode have to be satisfied [31]

$$\Phi(\omega)=\phi_{bottom\_DBR}(\omega)+\phi_{top\_DBR}(\omega)+2N_{QW}h_{QW}k_R^{(QW)} + 2(N_{QW}+1)h_bk_R^{(b)}+\sum_{n\in cladding}2h_nk_R^{(n)}=2m\pi \quad (1)$$

$$G(g)=\sum_{n\in QWs}2h_n\Gamma_{L,n}(\omega)g_{M,n}-\sum_n 2h_n\Gamma_{L,n}(\omega)\alpha_{i,n}(\hbar\omega) - \ln\left(\frac{1}{|r_{bottom\_DBR}(\omega)|^2\left|r_{top\_DBR}(\omega)\right|^2}\right)=0 \quad (2)$$

where ω is optical frequency, h_{QW}, h_b, and h_n are the thickness of the quantum wells, the barriers, and the segments in the cladding layers, respectively. $k_R^{(QW)}$, $k_R^{(b)}$, and $k_R^{(n)}$ are the real part of the propagation constant in quantum wells, barriers, and cladding layers, respectively. $\Gamma_{L,n}$ is the longitudinal optical confinement factor. N_{QW} is the number of quantum wells. The schematic layer structure is shown in Fig. 2. The resonant (lasing) wavelength is determined by the phase condition in Eq. (1). Note that the effective indices for the top DBRs are simply refractive indices of materials since there is no waveguide in that region. The threshold material gain (g) can be obtained through the threshold modal gain condition, Eq. (2), when the cavity modal gain is balanced by the sum of the intrinsic and mirror losses. Since the scattering loss in the interface between the pillar and substrate is ignored in Eq. (2), the calculated gain will be underestimated. Nevertheless, this approach gives almost the same resonant wavelength as that from the finite-difference time domain method (FDTD), and is able to show the alignment of the standing wave pattern with the quantum wells under the resonance condition. More details can be found in [31].

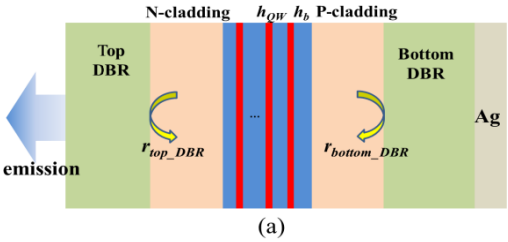

Fig. 2 The layer structure, sandwiched between two DBR regions, applied to the lasing threshold condition.

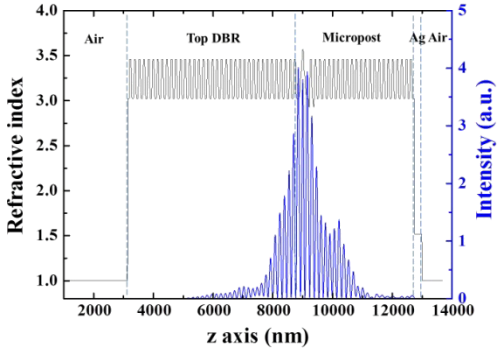

Fig. 3 The standing wave pattern calculated from the FDTD method. The field is confined in MQW's region and decays into DBR regions.

Once the resonant wavelength and the location of the peaks of the standing wave are found, we use FDTD to obtain more accurate parameters such as the quality factor, Q, wave pattern, and energy confinement factor, Γ_E. We place a dipole source with the wavelength obtained from Eq. (1) at the proper position to excite HE_{11} mode. The standing wave pattern is shown in Fig. 3. Q and Γ_E are 1,745 and 0.021, respectively. Thus, the threshold material gain is 7,241 cm^{-1} according to $g_{th}=\omega/(\Gamma_E v_g Q)$, where ω. is the resonance frequency and v_g is the group velocity [21]. The light output power versus injection current (L-I) curve can be solved through the rate equations, as described in Sect. 2(b) next.

2.2 Rate Equations for Nanolasers

The rate equations for a laser cavity with the presence of metal have to be dealt with carefully. Metals function as plasmas in the optical frequency regime, implying that they are lossy, dispersive, and the real part of the permittivities can become negative. The issue for modeling a metal-cavity nanolaser involves how to normalize the optical field such that the total electromagnetic energy is one photon energy [21]. The optical field normalization is needed to obtain physically meaningful spontaneous and stimulated emission rates. The energy confinement factor should be used instead of the commonly used power confinement factor since the Poynting's vector can be negative in the plasma region when the permittivity becomes negative and dispersive [22], [23]. The rigorous rate equations used for metal cavity nanolasers are presented below:

$$\frac{\partial n}{\partial t} = \frac{1}{qV_a}(\eta_i I - I_l) - R_{nr}(n) - R_{sp}(n) - R_{st}(n)S(n) \quad (3)$$

$$\frac{\partial S}{\partial t} = -\frac{S}{\tau_p} + \Gamma_E \beta_{sp} R_{sp}(n) + \Gamma_E R_{st}(n)S(n) \quad (4)$$

where

n = carrier density (cm^{-3})
I = injection current (A)
η_i = injection efficiency
q = electron charge (Coulomb)
V_a = active material volume (cm^{-3})
$R_{nr}(n)$ = nonradiative recombination rate ($\text{s}^{-1}\text{cm}^{-3}$)
$R_{sp}(n)$ = spontaneous emission rate ($\text{s}^{-1}\text{cm}^{-3}$)
$R_{st}(n)$ = stimulated emission coefficient (s^{-1})
$S(n)$ = photon density (cm^{-3})
I_l = leakage current (A)
τ_p = photon life time (s)
Γ_E = optical energy confinement factor
β_{sp} = spontaneous emission coupling factor

The nonradiative recombination rate accounting for the surface recombination and Auger recombination is:

$$R_{nr}(n) = v_s \frac{A_a}{V_a} n + Cn^3 \quad (5)$$

where

v_s = surface velocity (cm/s)
A_a = the surface area of the active material (cm^2)
C = Auger recombination coefficient (cm^6s^{-1}).

The spontaneous emission rate coupling to the continuum modes and the m-th cavity mode is

$$R_{sp}(n) = R_{sp,c}(n) + R_{sp,m}(n) \quad (6)$$

The first term is spontaneous emission rate coupling into the continuum modes and is defined as:

$$R_{sp,c}(n) = \frac{1}{\tau_{sp,rad}} \frac{1}{V_a} \sum_{\mathbf{k}} f_{c,k}(1 - f_{v,k}) \quad (7)$$

where

$\tau_{sp,rad}$ = radiative life time (s)
$f_{c,k}$ = Fermi-Dirac occupation probability of electrons in the conduction band
$f_{v,k}$ = Fermi-Dirac occupation probability of electrons in the valence band.

The second term is spontaneous emission rate coupling in a specific (m-th) cavity mode and is defined as:

$$\begin{aligned} R_{sp,m}(n) &= \beta_{sp} R_{sp}(n) \\ &= \frac{\Gamma_E}{V_a} \frac{2\pi^2 q^2}{\varepsilon_0 \left(\varepsilon_{R,a}(\omega_m) + \varepsilon_{g,a}(\omega_m)\right) m_0^2 \omega_m} \int d\omega \frac{1}{\pi} \frac{\Delta\omega_m}{(\omega - \omega_m)^2 + \Delta\omega_m^2} \\ &\quad \times \frac{1}{V_a} \sum_{\mathbf{k}} |\hat{e} \cdot \vec{p}_k|^2 \frac{\gamma}{\pi} \frac{f_{c,k}(1 - f_{v,k})}{(E_{c,k} - E_{v,k} - \hbar\omega)^2 + \gamma^2} \end{aligned} \quad (8)$$

where

$\varepsilon_{R,a}$ = the real part of the relative permittivity in the active region
$\varepsilon_{g,a}$ = the real part of the relative group permittivity in the active region
$|\hat{e} \cdot p_k|$= the optical momentum matrix element (kgcm/s)
γ = the linewidth of optical transition (eV)
v_g= the group velocity (cm/s)
V_{eff} = the effective modal volume (cm^{-3})
n_{eff} = the effective index of the mode.

The optical energy confinement factor should be used for dispersive media:

$$\Gamma_E = \frac{\int_{V_a} d\mathbf{r} \frac{\varepsilon_0}{4} \left[\varepsilon_g(\mathbf{r}, \omega_m) + \varepsilon_R(\mathbf{r}, \omega_m)\right] |\mathbf{E}(\mathbf{r})|^2}{\int_V d\mathbf{r} \frac{\varepsilon_0}{4} \left[\varepsilon_g(\mathbf{r}, \omega_m) + \varepsilon_R(\mathbf{r}, \omega_m)\right] |\mathbf{E}(\mathbf{r})|^2} \quad (9)$$

where the relative "group permittivity," $\varepsilon_g(\mathbf{r}, \omega_m)$, is

$$\varepsilon_g(\mathbf{r}, \omega_m) = \frac{\partial[\omega \varepsilon_R(\mathbf{r}, \omega)]}{\partial\omega} \Big|_{\omega=\omega_m} \quad (10)$$

and $\mathbf{E}(\mathbf{r})$ is the optical electric field at $\omega = \omega_m$.

Finally, the stimulated emission coefficient is

$$R_{st}(n) = v_g g(n) \quad (11)$$

where

v_g = group velocity (cm/s)
$g(n)$ = gain coefficient (cm^{-1})

In addition, we take into account the leakage current I_l, which can be approximated as [32]:

$$I_l = I_0 \exp[-(E_{conf,g} - \Delta F)/k_b T] \quad (12)$$

where $E_{conf,g}$ and ΔF are the band gap energy of the electron confinement layer in the active region of the laser and the separation of quasi-Fermi levels in the conduction and valence bands, respectively [32]. I_0 is a fitting parameter. Clearly, I_l is proportional to thermionic emission rate in the gain medium and it increases with carrier density, i.e. a larger ΔF, and temperature. Due to the current leakage, the carrier density is not completely pinned with increasing bias current even after the threshold condition is reached.

In addition, we use the 4×4 Luttinger-Kohn Hamiltonian under the axial approximation [33] to calculate the optical gain spectra of the active region consisting of 5 pairs of $In_{0.21}Ga_{0.79}As$ (4.2 nm)/$Ga_{0.12}As_{0.88}P$ (6 nm) quantum wells at various carrier densities. Due to the thin barrier thickness, the wave function coupling among quantum wells occurs and this effect is taken into account in our gain model.

3. Metal Cavity Surface-Emitting Microlasers

For our metal-cavity surface-emitting microlaser [27], as illustrated in Fig. 1, optical feedback is provided by a bottom 23-pair and a top (emission side) 33-pair $Al_{0.9}Ga_{0.1}As/Al_{0.12}Ga_{0.88}As$ quarter-wavelength DBR layers. Multiple quantum wells composed of 5 pairs of $In_{0.21}Ga_{0.79}As$ (4.2 nm) quantum wells and $GaAs_{0.88}P_{0.12}$ (6 nm) barriers under the strain balance condition are used in the active region. The fundamental HE_{11} mode preserves the circular beam shape and a null-free emission pattern [27]. The round-trip phase shift is tuned to match the resonance condition according to Eq. (1) through the introduction of metal dispersion and modal characteristics into the effective index. Phase shifts from the imperfect reflection of metal/semiconductor interface are included for the resonance wavelength prediction. The threshold material gain g_{th} is estimated as described in Sect. 2.

Lithography and dry etching are used to create the micropost structure. A silver coating is performed by e-beam evaporation after the sidewall passivation of SiN_x. The micropost has a radius of $\sim$1.0 μm and a height of $\sim$4.0 μm just through the active region. A complete removal of the original GaAs substrate by wet etching and flip-chip bonding to silicon are used to transfer the devices. The etching stops right at the exposure of the DBR layers where an n-contact was deposited. In Figs. 4(a) and (b), the device shows a lasing wavelength of 995 nm and a clear threshold of 2.6 mA in the light output power vs. injection current (L-I curve) with CW operation at room temperature. The output power goes to 8 μW at a bias current of 4 mA.

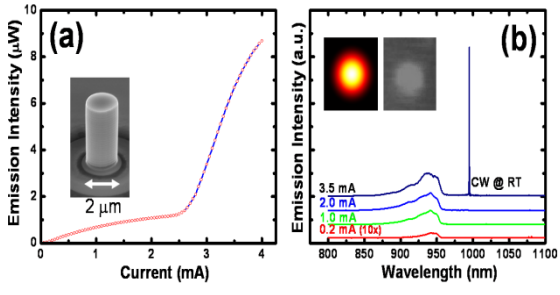

Fig. 4 (a) The L-I curve under CW current injection with a threshold around 2.6 mA at room temperature. The emission power can go up to more than 8 μW. (Inset: A SEM micrograph of a 2 μm-diameter cavity before insulator encapsulation.) (b) The corresponding spectra under different biases. A clear lasing peak at 995 nm was observed. (Inset: The cross-section electric field squared $|E|^2$ inside the active region calculated by the finite element method and the infrared camera image while operating [27].)

4. Comparison between Theory and Experiment

To calculate the light output power vs. current (L-I curve) and compare it with the experimental data, the thermal effect has to be considered in the rate equations. Thus, a self-consistent model has to be used, i.e., the power difference between the electrical and optical power contributes to heat dissipation and leads to increase of temperature inside the device. Therefore, leakage current, spontaneous emission and stimulated emission not only vary with carrier density but also temperature. Moreover, the high carrier density and temperature increase redshift the optical transition energy due to two mechanisms: one is band gap renormalization from many-body effects and the second is the band gap change from material lattice constant change with temperature.

To take these two affects into account, the reduction of energy difference for each optical transition (5 transitions due to coupling among 5 MQW's), ΔE_g, is modeled as:

$$\Delta E_g = -a(T - T_{\text{sink}}) - \Delta E_{BR}\tilde{n}^c \tag{13}$$

where T and T_{sink} are the temperature inside the active region and the temperature set in the heat sink, which is 300 K in the case, respectively, and $\tilde{n}$ is surface carrier density normalized to 1×10^{12} cm^{-2}. Note that the carrier density is the total carrier density within 5 quantum wells. The first term represents the effect of material band gap change with temperature and the second term is due to band gap renormalization. a can be extracted from Hamiltonian calculation. As for the band gap renormalization, it is widely believed that ΔE_g approximately depends on the carrier density n with power of third order. However, the screening effect in $In_xGa_{1-x}As$/InGaAsP latticed matched to GaAs for 980 nm laser system can alleviate the band gap shrinkage from band gap renormalization at high carrier density [34], which means that with the consideration of the screening effect, the band gap shrinkage is not as significant as expected. Based on the above discussions, we use: $a = 0.43$ meV/K, $\Delta E_{BR} = 9.759$ meV, and c = 0.52. The dependence of electron confinement layer, $Al_{0.35}Ga_{0.65}As$, on temperature [35] is also considered in the leakage current. Figure 5 shows the comparison between theory and experiment of the L-I curve, and an excellent agreement is demonstrated.

In our calculation, the surface velocity is set as 1.01×10^5 cm/s, $\tau_{sp,rad} = 2.8$ ns, C = 1.31×10^{-29} cm^6/s, and $\eta_i = 0.58$. The collection efficiency is used to match the theoretical optical output power with the experiment data.

Furthermore, the power from the spontaneous emission is also included in our theoretical L-I curve. A concave curve below the threshold current can be observed in Fig. 5. The reason is that in the long wavelength, Auger recombination can be significant and dominate in the injection current at high bias. Thus, the current is proportional to n^3 at high current injection. On the other hand, the light power below the threshold condition is from spontaneous emission, which is approximately proportional to n^2. Thus, the light

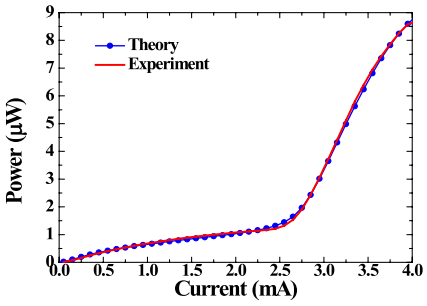

Fig. 5 The comparison between theoretical L-I curve (blue dot curve) and experimental curve (red curve). The threshold current I_{th} is around 2.5 mA.

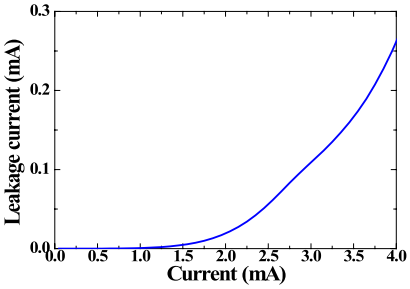

Fig. 7 The leakage current increases versus injection current. Due to increase of carrier density and temperature, leakage current increases exponentially in high bias.

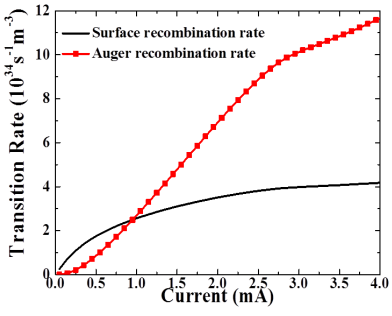

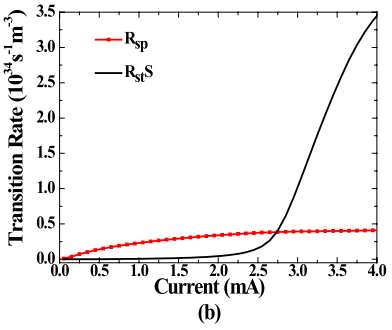

Fig. 6 (a) The surface recombination rate (black curve) and Auger recombination rate (red dot curve). (b) The stimulated emission ($R_{st}S$) and spontaneous emission (R_{sp}) rates. The former surpasses the latter at around 2.75 mA.

output power below threshold condition is proportional to current with the dependence of $I^{2/3}$.

To further verify this concept, the surface and Auger recombination rates are shown in Fig. 6(a). At low current injection, the surface recombination rate is larger than the Auger recombination rate. With increase of current, Auger recombination rate dominates the nonradiative recombination process and results in the concave curve below threshold. In addition, the stimulated emission and spontaneous emission rates are plotted in Fig. 6(b). An intentional detuning of 15 nm is designed in this layer structure with the consideration that the gain peak alignment with the cavity resonant wavelength at high bias.

The stimulated emission surpasses the spontaneous emission around 2.75 mA. Furthermore, the different scales in Figs. 6(a) and 6(b) show the nonradiative recombination rate dominates the injection current. The surface recombination rate depends on the ratio of active material area to volume, which is two over radius for cylinder, and the surface velocity. The large ratio of the surface area to volume is inevitable in nanolasers and thus, the reduction of surface velocity is necessary for decreasing threshold current. This can be improved either by using a better passivation or making devices work at lower temperatures. To reduce the Auger recombination, one method is to use a wide band gap material or to reduce the threshold material gain, and hence, the carrier density to alleviate Auger recombination rate.

In addition, the increase of carrier density even after threshold current is clearly seen in Fig. 6(a). The clear turning point after threshold current is apparent for Auger recombination rate since it is proportional to cube of n. The smaller slope in the Auger recombination rate after threshold implies the slow increase in carrier injection and the linearity also means Auger recombination rate dominates the current at higher bias. The reason that the carrier density is not pinned is that with increase of temperature, the quasi-Fermi distribution starts to broaden and reduces the electron and hole occupation probabilities in the transition energies. Therefore, a larger carrier density is needed to maintain the modal gain to overcome the total loss. However, this mechanism leads to a larger Fermi energy separation, ΔF. In conjunction with the increase of temperature, these two effects enhance the increase of leakage current, which results in the rollover of the L-I curve at high bias. Figure 7 shows the trend and the leakage current increases from a negligible scale to 0.25 mA as injection current increases. According to our model, the temperature inside the laser increases from 300 K to 335 K during the operation.

The extraction of spontaneous emission coupling factor β can be carried out from the ratio of $\beta R_{sp}(n)$ over $R_{sp}(n)$; and it obviously depends on the carrier density. Figure 8 shows β as a function of the injection current. Since both $\beta R_{sp}(n)$ and $R_{sp}(n)$ increase with current, there is a maximum value of β before threshold, which is around 0.65 mA in this case. It increases when the $\beta R_{sp}(n)$ starts to increase while $R_{sp}(n)$ increases gradually. After the threshold, $R_{sp}(n)$ keeps increasing due to thermal effect but $\beta R_{sp}(n)$ is saturating, which makes β gradually decrease. The β value around

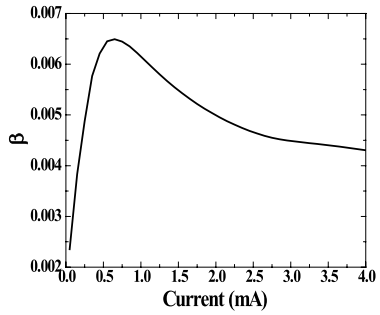

Fig. 8 The spontaneous emission coupling factor β as a function of current. Around the threshold at 2.75 mA, β is around 0.45%.

threshold current is 0.45%. This number can be further improved by increasing the energy confinement factor.

5. Further Size Reduction: Metal-Cavity Surface-Emitting Nanolasers and NanoLEDs

Toward nanoscale lasers with further reduction in the cavity volume, we have fabricated metal encapsulated nano-cavity light emitting diodes, which operate with electrical injection at room temperature. Figure 9(a) shows a schematic diagram of our fabricated nanoLED [28], where the active region is a bulk InGaAs layer with InP cladding. The cavity height of this device is designed as 200 nm, leading to a fundamental HE_{111} mode. Figures 9(b)–(d) show SEM images of the key steps in device fabrication. The metal-defined nanocavity has a total layer thickness of 200 nm and a radius with the smallest of 750 nm. The sidewall of the disk is passivated with SiN_x before metallization. This layer serves as a sidewall passivation, electrical isolation, and optical cladding layer between the active region and the surrounding metal. The smallest cavity volume encapsulated by silver is about 0.45 μm^3, which corresponds to 0.11 λ_0^3 in terms of the free space wavelength.

The I-V curve, Fig. 10(a), indicates good electrical isolation between anode and cathode by the thin 100 nm silicon nitride layer. It shows an excellent diode turn-on voltage at 1.06 V. The L-I curves show a slope efficiency of 0.27 mW/A at 28°C and 0.31 mW/A at 15°C. The electrical injection spectra, Fig. 10(b), show no degradation compared with photoluminescence (PL) spectrum from wafer before processing, but we could not observe cavity mode or spectrum narrowing from this device. This is because a subwavelength metal cavity suffers too large radiation loss as well as metal loss at room temperature.

In order to improve the quality factor, we have also designed a larger cavity metal encapsulated device in an attempt to fabricate a laser. The device structure is similar to Fig. 11(a) except that the height is 1.599 μm, which is about six times of the previous design. This is designed such that the fundamental HE_{11} mode has six standing wave peaks along the vertical direction (HE_{116}). The cavity dimension is designed in the same way as Eq. (1) with special attention on the phase shift and magnitude with the metal

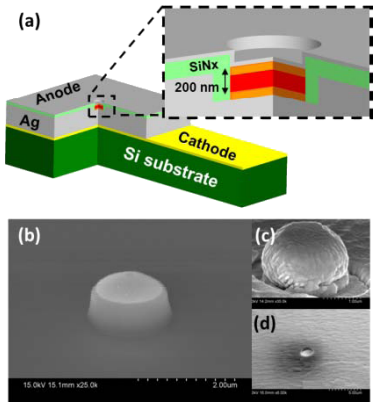

Fig. 9 (a) Schematic diagram of the metal-cavity surface-emitting nanoLED. The whole InP(p)-InGaAs(i)-InP (n) is encapsulated by metal with a thin SiN_x interface layer to avoid short circuit [28]. (b) SEM device picture after SiN_x deposition for isolator between anode and cathode together with sidewall passivation, (c) conformal Ag covering, and (d) finished device after flip-chip bonding and substrate removal.

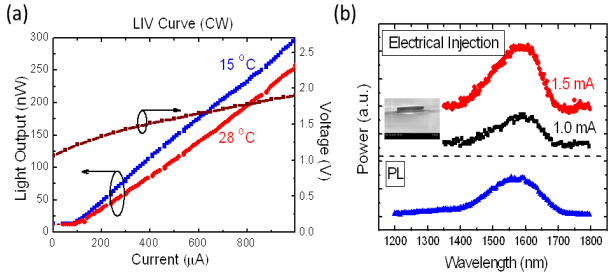

Fig. 10 (a) The light output and voltage vs. current curves [28], and (b) electroluminescence and photoluminescence spectra for nano-LED with radius of 1.0 μm (cavity volume of 0.76 μm^3 or 0.19 λ_0^3) at room temperature.

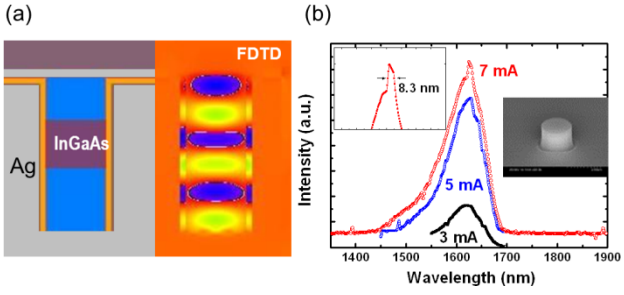

Fig. 11 (a) The structure of the device with InGaAs as the active material and the corresponding FDTD calculation showing the electric field distribution inside the cavity. (b) Current-dependent spectra for a device height of 1.599 μm. (c) The spectra compared with the epi-wafer photoluminescence (PL), 200 nm height device, and 1.599 μm height device, showing spectral narrowing from $\Delta\lambda$ = 190 nm to 8.3 nm.

reflector, which is a function of the metal thickness. Figure 11(a) shows the device structure and the corresponding FDTD calculation showing the electric field distribution inside the cavity for the HE_{116} mode. The resonant wavelength of our numerical FDTD result agrees well with the simple Fabry-Perot design result in Sect. 2. Figure 11(b) shows the optical spectra of the metal-cavity electrical in-

jection emitters at room temperature. The cavity was fabricated with a radius of 1 μm and a height of 1.599 μm, corresponding to a volume of 1.23 λ_0^3. Room temperature spectrum narrowing was observed with this device. Spectral narrowing from $\Delta\lambda$ = 190 nm (wafer PL spectrum) to 8.3 nm was observed with the increase of the current injection. So far, the room-temperature performance of 3D-confined subwavelength lasers was achieved mostly by optical pumping [16], [17] with a recent electrical injection laser at low temperature [15]. Our preliminary successful demonstration of a metal-encapsulated nano-cavity emitter at room temperature paves the way toward the realization of electrical injection nanolasers.

6. Conclusion and Future Work

In conclusion, we have presented a rigorous model and demonstrated experimentally room-temperature metal-cavity surface-emitting microlasers and nanoLEDs. Our theory explains the measured light output power vs. injection current (L-I curve) of the microlasers very well and identifies the relative contributions of radiative and non-radiative (Auger and defect) recombination rates as well as leakage current. Our smaller nano-coin structures [30], shown in Fig. 1(b), exhibit LED performance as described in Sect. 5. The metal reflectors are designed to replace or integrate with the reduced number of DBR pairs based on our strategy. A pure metal mirror without the DBR can be used, provided that special care is taken with the design of its thickness. To have a good laser output power, the thickness of metal reflector should be optimized. We have demonstrated the successful coating of a thin metal layer as an output coupling mirror in the nano-LED, moving toward the realization of a nano-coin laser [30].

Nanolasers pose challenges for researchers in photonics, both intellectually and technologically. Due to their compactness in size and substrate-free, silicon compatibility, it is promising to bridge the gap between photonics and silicon electronics. They have potential applications for ultra-high density photonic integrated circuits with ultralow power consumption and ultra-small footprint and ultrafast switching speed. The prototype of our design, with its transferability, metal-shielding, and energy efficiency, combined with existing technology, would bring a new application platform. The process is scalable down to subwavelength fabrication. Further research is necessary to reduce the metal losses in the cavity and to overcome the technological challenges of nanofabrication.

Acknowledgments

We thank our collaborators S.W. Chang formerly at UIUC, U.S.A.; T.D. German, A. Mutig, U. Pohl, and D. Bimberg at Technical University of Berlin, Germany. We also thank L. Zhang at Bell Laboratories, Alcatel-Lucent for crystal growth of the nanoLED *epi*-wafers. This work was supported by DARPA NACHOS program in USA.

References

[1] R.G. Beausoleil, P.J. Kuekes, G.S. Snider, S.Y. Wang, and R.S. Williams, "Nanoelectronic and nanophotonic interconnect," Proc. IEEE, vol.96, no.2, pp.230–247, Feb. 2008.

[2] D.A.B. Miller, "Device requirements for optical interconnects to silicon chips," Proc. IEEE, vol.97, no.7, pp.1166–1185, July 2009.

[3] M.T. Hill, "Status and prospects for metallic and plasmonic nanolasers," J. Opt. Soc. Am. B, vol.27, no.11, B36-B44, 2010.

[4] T.H. Maiman, "Stimulated optical radiation in ruby," Nature, vol.187, no.4736, pp.493–494, Aug. 1960.

[5] R.N. Hall, G.E. Fenner, J.D. Kingsley, T.J. Soltys, and R.O. Carlson, "Coherent light emission from GaAs junctions," Phys. Rev. Lett., vol.9, no.9, pp.366–368, Nov. 1962.

[6] M.I. Nathan, W.P. Dumke, G. Burns, F.H. Dill, Jr., and G. Lasher, "Stimulated emission of radiation from GaAs p-n junctions," Appl. Phys. Lett., vol.1, no.3, pp.62–64, Nov. 1962.

[7] N. Holonyak, Jr. and S.F. Bevacqua, "Coherent (visible) light emission from $GaAs_{1-x}P_x$ junctions," Appl. Phys. Lett., vol.1, no.2, pp.82–83, Oct. 1962.

[8] T.M. Quist, R.H. Rediker, R.J. Keyes, W.E. Krag, B. Lax, A.L. McWhorter, and H.J. Zeiger, "Semiconductor maser of GaAs," Appl. Phys. Lett., vol.1, no.4, pp.91–92, Dec. 1962.

[9] H. Soda, K. Iga, C. Kitahara, and Y. Suematsu, "GaInAsP/InP surface emitting injection lasers," Jpn. J. Appl. Phys., vol.18, no.6, pp.2329–2330, June 1979.

[10] A.F.J. Levi, R.E. Slusher, S.L. McCall, T. Tanbun-Ek, D.L. Coblentz, and S.J. Pearton, "Room temperature operation of microdisk laser with submilliamp threshold current," Electron. Lett., vol.28, no.11, pp.1010–1012, May 1992.

[11] H.G. Park, S.H. Kim, S.H. Kwon, Y.G. Ju, J.K. Yang, J.H. Baek, S.B. Kim, and Y.H. Lee, "Electrically driven single-cell photonic crystal laser," Science, vol.305, no.5089, pp.1444–1447, Sept. 2004.

[12] M.T. Hill, Y.S. Oei, B. Smalbrugge, Y. Zhu, T. de Vries, P.J. van Veldhoven, F.W.M. van Otten, T.J. Eijkemans, J.P. Turkiewicz, H. de Waardt, E.J. Geluk, S.H. Kwon, Y.H. Lee, R. Notzel, and M.K. Smit, "Lasing in metallic-coated nanocavities," Nature Photon., vol.1, no.10, pp.589–594, Oct. 2007.

[13] M.T. Hill, M. Marell, E.S.P. Leong, B. Smalbrugge, Y. Zhu, M. Sun, P.J. van Veldhoven, E.J. Geluk, F. Karouta, Y. Oei, R. Nötzel, C.Z. Ning, and M.K. Smit, "Lasing in metal-insulator-metal subwavelength plasmonic waveguides," Opt. Express, vol.17, no.13, pp.11107–11112, June 2009.

[14] K. Ding, Z. Liu, L. Yin, H. Wang, R. Liu, M.T. Hill, M.J. H. Marell, P.J. van Veldhoven, R. Nötzel, and C.Z. Ning, "Electrical injection, continuous wave operation of subwavelength-metallic-cavity lasers at 260 K," Appl. Phys. Lett., vol.98, no.23, 231108, June 2011.

[15] J.H. Lee, M. Khajavikhan, A. Simic, Q. Gu, O. Bondarenko, B. Slutsky, M.P. Nezhad, and Y. Fainman, "Electrically pumped subwavelength metallo-dielectric pedestal pillar lasers," Opt. Express, vol.19, no.22, pp.21524–21531, Oct. 2011.

[16] K. Yu, A.M. Lakhani, and M.C. Wu, "Subwavelength metal-optic semiconductor nanopatch lasers," Opt. Express, vol.18, no.9, pp.8790–8799, April 2010.

[17] S.H. Kwon, J.H. Kang, C. Seassal, S.K. Kim, P. Regreny, Y.H. Lee, C.M. Lieber, and H.G. Park, "Subwavelength plasmonic lasing from a semiconductor nanodisk with silver nanopan cavity," Nano Lett., vol.10, no.9, pp.3679–3683, Aug. 2010.

[18] M.P. Nezhad, A. Simic, O. Bondarenko, B. Slutsky, A. Mizrahi, L. Feng, V. Lomakin, and Y. Fainman, "Room-temperature subwavelength metallo-dielectric lasers," Nat. Photon., vol.4, pp.395–399, April 2010.

[19] A.M. Lakhini, M. Kim, E.K. Lau, and M.C. Wu, "Plasmonic crystal defect laser," Opt. Express, vol.19, no.19, pp.18237–18245, Sept. 2011.

[20] X. Yang, A. Ishikawa, X. Yin, and X. Zhang, "Hybrid photonic plas-

monic crystal nanocavities," ACS Nano., vol.5, no.4, pp.2831–2838, March 2011.
[21] S.W. Chang and S.L. Chuang, "Fundamental formulation for plasmonic nanolasers," IEEE J. Quantum Electron., vol.45, no.8, pp.1014–1023, Aug. 2009.
[22] S.W. Chang, T.R. Lin, and S.L. Chuang, "Theory of plasmonic Fabry-Perot nanolasers," Opt. Express, vol.18, no.14, pp.15039–15047, June 2010.
[23] S.W. Chang, C.Y.A. Ni, and S.L. Chuang, "Theory for bowtie plasmonic nanolasers," Opt. Express, vol.16, no.14, pp.10580–10595, July 2008.
[24] C.Y. Lu, S.W. Chang, S.L. Chuang, T.D. Germann, and D. Bimberg, "Metal-cavity surface-emitting microlaser at room temperature," Appl. Phys. Lett., vol.96, no.25, 251101, June 2010.
[25] C.Y. Lu, S.W. Chang, S.L. Chuang, T.D. Germann, U.W. Pohl, and D. Bimberg, "CW substrate-free metal-cavity surface microemitters at 300 K," Semicond. Sci. Technol., vol.26, no.1, pp.014012–014018, Nov. 2011.
[26] C.Y. Lu, S.W. Chang, S.L. Chuang, T.D. Germann, U.W. Pohl, and D. Bimberg, "Low thermal impedance of substrate-free metal cavity surface-emitting microlasers," IEEE Photonics Technol. Lett., vol.23, no.15, pp.1031–1033, Aug. 2011.
[27] C.Y. Lu, S.L. Chuang, A. Mutig, and D. Bimberg, "Metal-cavity surface-emitting microlaser with hybrid metal-DBR reflectors," Opt. Lett., vol.36, no.13, pp.2447–2449, June 2011.
[28] A. Matsudaira, C.Y. Lu, S.L. Chuang, and L. Zhang, "Demonstration of metallic nano-cavity light emitters with electrical injection," CLEO:2011 — Laser Applications to Photonic Applications, OSA Technical Digest (CD) (Optical Society of America, 2011), paper JMA5.
[29] M.T. Hill and M.J.H. Marell, "Surface-emitting metal nanocavity lasers," Adv. Opt. Technol., vol.2011, pp.314952–314959, July 2011.
[30] C.Y. Lu and S.L. Chuang, "A surface-emitting 3D metal-nanocavity laser: Proposal and theory," Opt. Express, vol.19, no.14, pp.13225–13244, June 2011.
[31] S.W. Chang, C.Y. Lu, S.L. Chuang, T.D. Germann, U.W. Pohl, and D. Bimberg, "Theory of metal-cavity surface-emitting microlasers and comparison with experiment," IEEE J. Sel. Top. Quantum Electron., vol.17, no.6, pp.1681–1692, Dec. 2011.
[32] P.W. Mena, J.J. Morikuni, S.M. Kang, A.V. Harton, and K.W. Wyatt, "A comprehensive circuit-level model of vertical-cavity surface-emitting lasers," J. Lightwave Technol., vol.17, no.12, pp.2612 – 2632, Dec. 1999.
[33] S.L. Chuang, Physics of Photonic Devices, 2nd ed., Chapter 4, Wiley, New York, 2009.
[34] S.H. Park and D. Ahn, "Screening effects on the bandgap renormalization of strained InGaAs/InGaAsP quantum well lasers lattice matched to GaAs," Appl. Phys. Lett., vol.68, no.13, pp.1844–1846, March 1996.
[35] S.A. Lourenço, I.F.L. Dias, J.L. Duarte, E. Laureto, E.A. Meneses, J.R. Leite, and I. Mazzaro, "Temperature dependence of optical transitions in AlGaAs," J. Appl. Phys., vol.89, no.11, pp.6159–6164, June 2001.

Shun Lien Chuang received the B.S. degree in electrical engineering from National Taiwan University in 1976, and the M.S., E.E., and Ph.D. degrees in electrical engineering from the Massachusetts Institute of Technology in 1980, 1981, and 1983, respectively. In 1983, he joined the faculty in the Department of Electrical and Computer Engineering at the University of Illinois at Urbana-Champaign, where he is currently the Robert MacClinchie Distinguished Professor since 2007. He was a visitor at AT&T Bell Laboratories (1989), the SONY Research Center (1995), and NTT Basic Research Laboratories (1997). He was also a visitor at NASA Ames Research Center (1999), Fujitsu Research Laboratories (2000), Cavendish Laboratory at the University of Cambridge (2002), and Technical University of Berlin (2009). He is conducting research on nanolasers, plasmonics, strained quantum-well and quantum-dot semiconductor lasers, and superlattice infrared photodetectors. He is the author of *Physics of Photonic Devices,* 2nd edition, 2009, (*Physics of Optoelectronic Devices*, first edition, 1995), Wiley, New York. He has published more than 400 journal and conference papers and given many invited talks at conferences and institutions. He served as an Associate Editor for the *IEEE Journal of Quantum Electronics (1997–2003)* and IEEE Journal of Lightwave Technology (2007–2008). He was a General Co-Chair for Slow and Fast Light Meeting of the Optical Society of America, July, 2008 and has served in many technical program committees of IEEE and Optical Society of America. He was a Feature Editor for a special issue in *Journal of Optical Society of America B* on *Terahertz Generation, Physics and Applications* in 1994. He also edited a feature section on Mid-Infrared Quantum-Cascade Lasers in the June 2002 issue of *the Journal of Quantum Electronics*. He is a Fellow of the American Physical Society, the IEEE, and the Optical Society of America. He has been cited many times for Excellence in Teaching at the University of Illinois. He was selected as an Associate at the Center for Advanced Study (campus honor) at the University of Illinois in 1995. He was awarded a Fellowship from the Japan Society for the Promotion of Science to visit the University of Tokyo in 1996. He received the Engineering Excellence Award from the Optical Society of America in 2004, the IEEE Lasers and Electro-Optical Society (LEOS) Distinguished Lecturer Award for 2004–2006, and the William Streifer Scientific Achievement Award from IEEE (LEOS) in 2007. He received the Humboldt Research Award for Senior US Scientists in 2008 and Microoptics Conference Award in 2011. He served as an elected member in the Board of Governors for the IEEE Photonics Society for 2009–2011.

Chi-Yu Ni received the B.S. degree in electrical engineering and the M.S. degree in photonics and optoelectronics from the National Taiwan University, Taipei, Taiwan, in 2000 and 2002, respectively. He is currently pursuing the Ph.D. degree in the Department of Electrical and Computer Engineering, University of Illinois at Urbana-Champaign, Urbana. His current research interests include semiconductor physics, mainly in optoelectronics, including plasmonic devices, lasers, and modulators.

Chien-Yao Lu received the B.S. and M.S. degrees in electrical engineering from the National Taiwan University, Taipei, Taiwan, in 2003 and 2005, respectively. He is currently working toward the PhD degree at the Department of Electrical and Computer Engineering, University of Illinois at Urbana-Champaign, USA. He is conducting research on the design, fabrication, and characterization of nanophotonic and plasmonic devices. During the Ph.D. study, he has designed and fabricated several metal-cavity lasers, including the devices used in this paper. His work on substrate-free metal-cavity microlasers won the best poster award (1st place) in international Nano-Optoelectronics Workshop (i-NOW) 2010. He was the recipient of the Nick and Katherine Holonyak, Jr. Outstanding Research Award from the Department of Electrical and Computer Engineering, University of Illinois at Urbana-Champaign and the Bor-Uei Chen Memorial Scholarship Award from the Photonics Society of Chinese-Americans in 2011.

Akira Matsudaira received his B.S. degree from Purdue University in 2006 and M.S. degree from University of Illinois Urbana-Champaign in 2008. He is currently pursuing his Ph.D. degree under the supervision of Professor S.L. Chuang in the Department of Electrical and Computer Engineering at the University of Illinois. His research includes designing, fabrication and characterization of optoelectronic devices. He is especially interested in physics of slow light in semiconductor optical amplifier, high speed characterization of integrated photonic devices, and fabrication of practical metal cavity semiconductor nanolasers.